Available online at website: https://journal.bcrec.id/index.php/bcrec

Bulletin of Chemical Reaction Engineering & Catalysis, 21 (1) 2026, 149-167

Original Research Article

# $NaHCO_3$-Assisted Synthesis of Ni-Promoted Sulfated Mesoporous Silica for the Hydrocracking of Used Cooking Oil into Biogasoline

**Karna Wijaya[1*], Marini Fairuz Vebryana[1], Niko Prasetyo[1], Aldino Javier Saviola[1], Wahyu Dita Saputri[2], Amalia Kurnia Amin[3], Latifah Hauli[4], Saharman Gea[5]**

*[1]Department of Chemistry, Faculty of Mathematics and Natural Sciences, Universitas Gadjah Mada, Yogyakarta 55281, Indonesia.*
*[2]Research Center for Hydrodynamics Technology, National Research and Innovation Agency (BRIN), The B. J. Habibie Science and Technology Area, South Tangerang, Banten 15314, Indonesia.*
*[3]Research Center for Catalysis, National Research and Innovation Agency (BRIN), The B. J. Habibie Science and Technology Area, South Tangerang, Banten 15314, Indonesia.*
*[4]Research Center for Molecular Chemistry, National Research and Innovation Agency (BRIN), The B. J. Habibie Science and Technology Area, South Tangerang, Banten 15314, Indonesia.*
*[5]Department of Chemistry, Faculty of Mathematics and Natural Sciences, Universitas Sumatera Utara, Medan 20155, Indonesia.*

*Received: 9th November 2025; Revised: 25th December 2025; Accepted: 26th December 2025*
*Available online: 28th December 2025; Published regularly: April 2026*

## Abstract

Biofuel production from biomass sources remains a key area of research, aimed at reducing reliance on fossil fuels and promoting environmental sustainability. This study investigates the conversion of used cooking oil (UCO) into biogasoline via catalytic hydrocracking, employing sulfated mesoporous silica dispersed with nickel as the catalyst. Mesoporous silica was synthesized using tetraethyl orthosilicate (TEOS) and $NaHCO_3$ as the template, followed by a hydrothermal method to introduce sulfate groups and nickel metal. Among the synthesized catalysts, SMS-2 exhibited the highest acidity across varying sulfuric acid concentrations, while 1 Ni/SMS-2 demonstrated superior acidity compared to other nickel loadings. The $SiO_2$, SMS-2, and 1 Ni/SMS-2 catalysts were evaluated for UCO hydrocracking in a semi-batch double-furnace reactor operated at an optimum temperature of 550 °C for 2 h, with a hydrogen flow rate of 20 mL.min$^{-1}$ under atmospheric pressure. Modifying mesoporous silica with sulfuric acid and nickel significantly enhanced its catalytic performance, with the 1 Ni/SMS-2 catalyst achieving the highest liquid product yield (66.10%) and gasoline fraction (35.47%) at an optimum catalyst-to-feed ratio of 1:100 (w/w). Notably, the resulting biogasoline exhibited a calorific value comparable to commercial gasoline and was free of aromatic hydrocarbons, indicating the potential for cleaner combustion. This study provides valuable insights into the effectiveness of mesoporous silica-based catalysts, highlighting their acid site modulation capabilities for efficiently transforming waste into high-value fuels.



***Keywords***: Biofuel production; catalytic hydrocracking; mesoporous silica; nickel; renewable energy

***How to Cite***: Wijaya, K., Vebryana, M. F., Prasetyo, N., Saviola, A. J., Saputri, W. D., Amin, A. K., Hauli, L., Gea, S. (2026). $NaHCO_3$-Assisted Synthesis of Ni-Promoted Sulfated Mesoporous Silica for the Hydrocracking of Used Cooking Oil into Biogasoline. *Bulletin of Chemical Reaction Engineering & Catalysis*, 21 (1), 149-167. (doi: 10.9767/bcrec.20531)

***Permalink/DOI***: https://doi.org/10.9767/bcrec.20531

## 1. Introduction

The transportation, industrial, and residential sectors remain highly energy dependent, with global demand continuing to rise because of population growth, technological advancement, and improved living standards. In 2021, global primary energy consumption reached approximately 14.21 gigatonnes of oil equivalent (Gtoe) [1]. Continued reliance on fossil fuels as the dominant energy source has raised serious concerns regarding resource depletion, environmental degradation, and long-term energy security. Excessive fossil fuel use is a major

* Corresponding Author.
Email: karnawijaya@ugm.ac.id (K. Wijaya)

contributor to climate change, air pollution, and greenhouse gas emissions. For example, motor vehicles in Pekanbaru City, Indonesia, emit approximately 788.50 tons of $CO_2$ per day [2], underscoring the severity of transport-related emissions in rapidly urbanizing regions. These challenges have intensified global efforts to transition toward sustainable and renewable energy systems, particularly in developing countries where energy security and environmental protection are closely linked.

Biofuels derived from waste resources have attracted growing interest due to their combined benefits of energy production and waste mitigation. Used cooking oil (UCO), a readily available waste stream generated by households, restaurants, and the food industry, represents a particularly promising feedstock. Improper disposal of UCO poses significant environmental risks, including water pollution and sewer blockage, while weak regulatory oversight in regions such as Yogyakarta, Indonesia, has led to uncontrolled trading and reuse [3]. Chemically, UCO is rich in triglycerides dominated by long-chain fatty acids, making it well-suited to produce gasoline-range hydrocarbons. Its valorization into biofuel, therefore, aligns with circular economy principles by improving resource efficiency, reducing waste generation, and minimizing competition with food resources [4].

Catalytic hydrocracking is recognized as one of the most effective routes for converting vegetable oil–based feedstocks into gasoline-range hydrocarbons under relatively moderate operating conditions [5]. This process enables simultaneous deoxygenation, cracking, and isomerization reactions, resulting in high-quality fuel products. Catalyst design plays a critical role in determining conversion efficiency, product selectivity, and resistance to deactivation, making the development of robust and highly active catalysts a key challenge in biofuel research.

Silica-based catalysts have received considerable attention for biofuel applications due to their low cost, high surface area, tunable porosity, and excellent thermal stability. Mesoporous silica materials, with pore diameters between 2 and 50 nm, offer improved mass transfer and accessibility for bulky triglyceride molecules during hydrocracking processes [6–8]. Various structure-directing agents have been employed to tailor mesoporous silica frameworks, including cetyltrimethylammonium bromide (CTAB) [9], cetyltrimethylammonium chloride (CTAC) [10], polyethylene glycol (PEG-400) [11], and Pluronic F108 [12]. In this study, sodium bicarbonate ($NaHCO_3$) was used as an environmentally benign pore-forming agent to synthesize mesoporous silica, followed by sulfation with sulfuric acid ($H_2SO_4$) to enhance acidity, pore volume, and pore diameter [13,14]. High surface acidity is essential for hydrocracking, as strong Brønsted acid sites promote C–C bond cleavage and skeletal isomerization [15]. Accordingly, sulfated catalysts have demonstrated excellent performance in a wide range of acid-catalyzed organic reactions [16-18].

Despite their strong acidity, sulfated mesoporous silica catalysts are prone to deactivation via coke formation, which compromises long-term stability. Incorporation of transition metals has therefore been widely explored to introduce hydrogenation functionality and suppress coke deposition. Nickel (Ni), an earth-abundant and cost-effective transition metal, exhibits high catalytic activity in hydrocracking [19], hydroisomerization [20], and hydrogenation reactions [21], making it particularly attractive for biofuel upgrading applications [22-24]. Our previous study [25] showed that a Ni-impregnated sulfated $ZrO_2$/pillared bentonite catalyst achieved a gasoline yield of 30.52% from coconut oil at 450 °C. Similarly, Riyandi *et al.* [26] reported that nickel supported on rice husk ash (Ni/RHA) converted oleic acid into bio-hydrocarbons with a conversion of 98.25% at 285 °C and 40 bar, further demonstrating the effectiveness of Ni-based catalysts in hydrocracking-based biofuel production.

To the best of our knowledge, the hydrothermal synthesis of nickel-impregnated sulfated mesoporous silica catalysts in the presence of $NaHCO_3$ for the conversion of UCO into biogasoline has not yet been reported. The hydrothermal approach employed in this work provides a controlled aqueous environment under elevated temperature and autogenous pressure, promoting homogeneous nucleation and uniform dispersion of nickel and sulfate species throughout the silica framework. Under these conditions, precursor species readily penetrate mesoporous channels and interact with surface silanol groups, resulting in well-dispersed active sites and enhanced structural stability. This strategy favors the incorporation of nickel and sulfate species within the internal pore network rather than on the external surface, thereby improving active-site accessibility and catalytic efficiency. Moreover, hydrothermal synthesis allows precise control over temperature, pH, and precursor concentration, minimizing particle agglomeration and yielding catalysts with uniform morphology and high phase purity. Compared with conventional mechanical stirring or wet impregnation methods, this approach is also more energy efficient and environmentally benign [27-29]. By comparison, Nadia *et al.* [30] reported that a NiMo-impregnated hierarchical silica catalyst prepared via conventional wet

impregnation produced only an 18.64% gasoline fraction from waste frying oil at 475 °C.

Accordingly, this study aims to advance the rational design of silica-based catalysts for sustainable biofuel production and to establish UCO as a viable and renewable feedstock for biogasoline synthesis. By integrating mesoporous silica architecture, sulfation-induced acidity, and nickel-based hydrogenation functionality through hydrothermal synthesis, this work seeks to develop an efficient and environmentally friendly hydrocracking process under atmospheric hydrogen pressure.

## 2. Materials and Methods

### 2.1 Materials

Mesoporous silica was synthesized using tetraethyl orthosilicate (TEOS, 98%, Merck), ethanol (99%, Merck), methanol (99%, Merck), hydrochloric acid (HCl, 37%, Mallinckrodt), sodium bicarbonate ($NaHCO_3$, 99%, Merck), and silver nitrate ($AgNO_3$, 99%, Merck). Sulfation was carried out using sulfuric acid ($H_2SO_4$, 98%, Smart Lab), while nickel was introduced from nickel(II) chloride hexahydrate ($NiCl_2 \cdot 6H_2O$, 99%, Merck). All chemicals were of analytical grade and used without further purification. Hydrogen ($H_2$) and nitrogen ($N_2$) gases were supplied by PT Surya Indotim Imex, and deionized water was obtained from OneMed.

Used cooking oil (UCO) collected from households was employed as the feedstock. Prior to analysis, the UCO was heated at 120 °C to remove residual moisture and subsequently centrifuged at 2000 rpm for 20 min to eliminate suspended impurities. Its physicochemical properties and fatty acid composition are summarized in Table 1. Commercial gasoline (Pertalite, RON 90) obtained from PT Pertamina was used as a reference fuel.

The physicochemical properties of the UCO, including acid value, saponification value, and free fatty acid (FFA) content, were determined using standard titration methods. The acid value was measured according to ASTM D664 using a standardized KOH solution in ethanol as the titrant and phenolphthalein as the indicator. The saponification value and FFA content were determined following ASTM D5558 and AOCS Cd 3d-63, respectively. For saponification value determination, the UCO sample was refluxed with an excess of alcoholic KOH solution, and the residual KOH was back-titrated with standardized HCl using phenolphthalein as the indicator. The FFA content was determined by titrating the oil sample with standardized KOH solution.

Table 1. Selected physicochemical properties of the UCO used in this study.

| Properties | Results |
|---|---|
| Acid value (mg KOH/g oil) | 4.8 |
| Saponification value (mg KOH/g oil) | 183.2 |
| FFA content (%) | 2.4 |
| *Fatty acid composition (%)* | |
| Myristic acid | 0.97 |
| Palmitic acid | 39.55 |
| Linoleic acid | 10.12 |
| Oleic acid | 45.17 |
| Stearic acid | 4.19 |
| Total fatty acid | 100 |

The fatty acid composition of the UCO was analyzed using a gas chromatography–mass spectroscopy (GC–MS, Shimadzu QP2010S) equipped with a DB-5MS capillary column (30 m × 0.25 mm × 0.25 μm). Prior to analysis, the UCO was esterified using methanol and concentrated $H_2SO_4$ as the catalyst to convert free fatty acids (FFAs) into fatty acid methyl esters (FAMEs) following a standard acid-catalyzed esterification procedure.

### 2.2. Synthesis of Mesoporous Silica

Mesoporous silica was synthesized via an acid-catalyzed sol–gel method using TEOS as the silica precursor. In a 250 mL beaker, 8.4 mL of TEOS was mixed with 0.795 g of $NaHCO_3$ and 15 mL of ethanol and stirred magnetically at 600 rpm. Separately, 15 mL of 2 M HCl was added dropwise at a rate of approximately one drop per second under continuous stirring to initiate TEOS hydrolysis and condensation, resulting in the formation of a white gel after approximately 1 h.

The gel was aged statically at room temperature for 12 h, centrifuged at 2000 rpm for 20 min, and washed repeatedly with deionized water until no turbidity was observed upon addition of $AgNO_3$ solution, confirming complete chloride removal. The washed gel was dried at 100 °C for 3 h and subsequently refluxed with 50 mL of methanol at 65 °C for 72 h in a 250 mL round-bottom flask under magnetic stirring. The solid product was then centrifuged, dried again at 100 °C for 3 h, and calcined at 500 °C for 4 h with a heating rate of 10 °C.min$^{-1}$ in air. The resulting white powder was sieved through a 270-mesh sieve and denoted as $SiO_2$.

### 2.3. Sulfation of Mesoporous Silica

Sulfation of mesoporous silica was performed following a modified hydrothermal procedure based on Pratika *et al.* [31]. Briefly, 5 g of $SiO_2$ was mixed with 50 mL of $H_2SO_4$ solution with concentrations of 1.0, 1.5, or 2.0 M and stirred at 600 rpm for 30 min in a Teflon-lined autoclave. The autoclave was then heated at 100 °C for 4 h.

The resulting solid was recovered by centrifugation at 2000 rpm for 20 min, dried at 120 °C for 3 h, and calcined at 500 °C for 4 h. The sulfated samples were designated SMS-1, SMS-1.5, and SMS-2 according to the $H_2SO_4$ concentration used. Their acidities were evaluated using ammonia temperature-programmed desorption ($NH_3$–TPD).

### 2.4. Nickel Impregnation onto Sulfated Mesoporous Silica

Nickel impregnation was performed on the most acidic sulfated mesoporous silica sample (SMS-X). Three grams of SMS-X was impregnated with 1, 2, or 3 wt% Ni using aqueous solutions of $NiCl_2.6H_2O$ dissolved in 50 mL of deionized water. The required amount of nickel precursor was calculated using Equation (1). The suspension was stirred for 30 min in a Teflon-lined autoclave and subsequently heated at 100 °C for 4 h. The solvent was then evaporated at 120 °C for 3 h. The impregnated samples were calcined at 500 °C for 4 h under a nitrogen flow of 20 mL.min$^{-1}$ and subsequently reduced at 500 °C for 4 h under hydrogen flow (20 mL.min$^{-1}$). The resulting catalysts were designated as 1 Ni/SMS-X, 2 Ni/SMS-X, and 3 Ni/SMS-X. Their acidities were further analyzed by $NH_3$–TPD.

$$\text{Mass of the } NiCl_2.6H_2O \text{ precursor} = \frac{\text{molecular mass of } NiCl_2{\cdot}6H_2O}{1\times\text{atomic mass of Ni}} \times C \times W \quad (1)$$

where $C$ is targeted metal concentration (wt%) and $W$ is mass of SMS-X matrix (g).

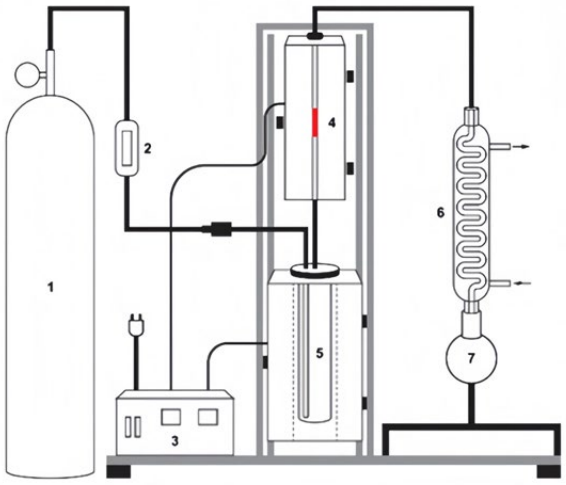


Figure 1. Schematic diagram of the hydrocracking reactor used in this study. (1) Hydrogen tank; (2) Flowmeter; (3) Thermocouple; (4) Catalyst furnace; (5) Feed furnace; (6) Condenser; (7) Liquid product container.

### 2.5. Hydrocracking of UCO

The optimum hydrocracking temperature was determined through non-catalytic thermal cracking experiments conducted at 500, 550, and 600 °C under a hydrogen flow rate of 20 mL.min$^{-1}$ for 2 h. The temperature yielding the highest liquid product fraction (550 °C) was selected for subsequent catalytic experiments. Catalytic hydrocracking was performed at 550 °C under continuous hydrogen flow (20 mL.min$^{-1}$) using $SiO_2$, SMS-2, and 1 Ni/SMS-2 as catalysts. The catalyst-to-feed ratio was fixed at 1:100 (w/w), corresponding to 0.1 g of catalyst per 10 g of UCO. Reactions were conducted in a semi-batch reactor equipped with a double-furnace system under atmospheric pressure for 2 h (Figure 1).

During operation, the catalyst placed in the upper chamber and the feedstock in the lower chamber were preheated to 200 °C. The temperature was then increased to 550 °C to vaporize the feed, allowing the vapors to pass through the catalyst bed under hydrogen flow. Liquid hydrocarbons, non-condensable gases, and coke were produced during the reaction. Reactor temperature was continuously monitored using a thermocouple positioned in contact with the reactor wall. The hydrogen flow rate and narrow reactor diameter ensured laminar gas flow, thereby minimizing external mass and heat transfer limitations and allowing the reaction rate to be governed primarily by intrinsic catalytic kinetics. The semi-batch, isothermal configuration minimized temperature gradients and ensured uniform reaction conditions.

Additional experiments using 1 Ni/SMS-2 were conducted at catalyst-to-feed ratios of 1:100, 2:100, and 3:100 (w/w). Product yields of liquid, gas, and coke were calculated using Equations (2)–(5). The gasoline, diesel, and non-hydrocarbon fractions in the liquid products were quantified by GC–MS analysis using Equations (5)–(7), where $A_g$, $A_d$, $A_n$, and $A_{total}$ represent the chromatographic peak areas of gasoline, diesel, non-hydrocarbons, and total components, respectively.

The liquid product exhibiting the highest gasoline yield was further characterized using Fourier transform infrared spectroscopy (FTIR, Thermo Scientific Nicolet iS10) and analyzed for calorific value using a Parr 6100 oxygen bomb calorimeter. The spent catalyst obtained after three consecutive reusability cycles was characterized by field-emission scanning electron microscopy coupled with energy-dispersive X-ray spectroscopy (FESEM–EDX) and transmission electron microscopy (TEM).

$$\text{Liquid product (wt\%)} = \frac{\text{weight of the liquid product (g)}}{\text{weight of feed (g)}} \times 100\% \quad (2)$$

$$\text{Coke (wt\%)} = \frac{(\text{weight of final catalyst} - \text{weight of initial catalyst})\ \text{g}}{\text{weight of feed (g)}} \times 100\% \quad (3)$$

$$\text{Gas (wt\%)} = 100\% - \text{liquid product} - \text{coke} \quad (4)$$

$$Y_{\text{g}}\ (\text{wt\%}) = \frac{A_{\text{g}}}{A_{\text{total}}} \times \frac{\text{weight of liquid product (g)}}{\text{weight of feed (g)}} \times 100\% \quad (5)$$

$$Y_{\text{d}}\ (\text{wt\%}) = \frac{A_{\text{d}}}{A_{\text{total}}} \times \frac{\text{weight of liquid product (g)}}{\text{weight of feed (g)}} \times 100\% \quad (6)$$

$$Y_{\text{n}}\ (\text{wt\%}) = \frac{A_{\text{n}}}{A_{\text{total}}} \times \frac{\text{weight of liquid product (g)}}{\text{weight of feed (g)}} \times 100\% \quad (7)$$

## 3. Results and Discussion

### 3.1. Functional Groups Identification of the Catalysts

The FTIR spectra of $SiO_2$, SMS-1, SMS-1.5, SMS-2, 1 Ni/SMS-2, 2 Ni/SMS-2, and 3 Ni/SMS-2 are presented in Figure 2. All samples exhibit characteristic absorption bands associated with the silica framework. The bands observed at approximately 467 $cm^{-1}$ and 802–805 $cm^{-1}$ are attributed to the bending and symmetric stretching vibrations of Si–O–Si bonds, respectively. In addition, the asymmetric stretching vibration of the Si–O–Si network appears in the range of 1088–1096 $cm^{-1}$, which is consistent with previously reported silica-based materials [32].

The broad absorption band detected at 3451–3458 $cm^{-1}$ corresponds to the stretching vibration of surface hydroxyl groups (Si–OH), while the band at 1636–1640 $cm^{-1}$ is assigned to the bending vibration of molecularly adsorbed water. These features indicate the presence of surface hydroxyl groups, which are known to play an important role in anchoring sulfate species and metal ions on the silica surface.

The presence of sulfate species is evidenced by absorption bands in the 950–1250 $cm^{-1}$ region, attributed to the stretching vibration of S–OH groups. This region overlaps with the asymmetric stretching vibration of Si–O–Si bonds, resulting in broadened and intensified bands. Such overlap arises from the coordination of sulfate ions with oxygen atoms on the silica surface, which lowers the symmetry of the sulfate complex and shifts its vibrational modes toward lower wavenumbers [33]. This observation confirms the successful sulfation of the silica support.

Notably, no distinct new absorption bands are observed after nickel impregnation. This absence may be attributed to the low nickel loading and the homogeneous dispersion of nickel species on the sulfated silica support, which limits the formation of bulk NiO phases detectable by FTIR. These results suggest that nickel incorporation does not significantly alter the fundamental silica framework or the coordination environment of sulfate species.

### 3.2. Acidity of the Catalysts

Catalyst acidity is a crucial factor in determining catalytic activity and selectivity for the hydrocracking process. Results of the $NH_3$–TPD analysis are summarized in Table 2, with

Table 2. Total acidity of the catalysts.

| Catalyst | Acidity (mmol/g $NH_3$) |
|---|---|
| $SiO_2$ | 0.273 |
| SMS-1 | 0.356 |
| SMS-1.5 | 0.442 |
| SMS-2 | 0.698 |
| 1 Ni/SMS-2 | 0.894 |
| 2 Ni/SMS-2 | 0.864 |
| 3 Ni/SMS-2 | 0.797 |

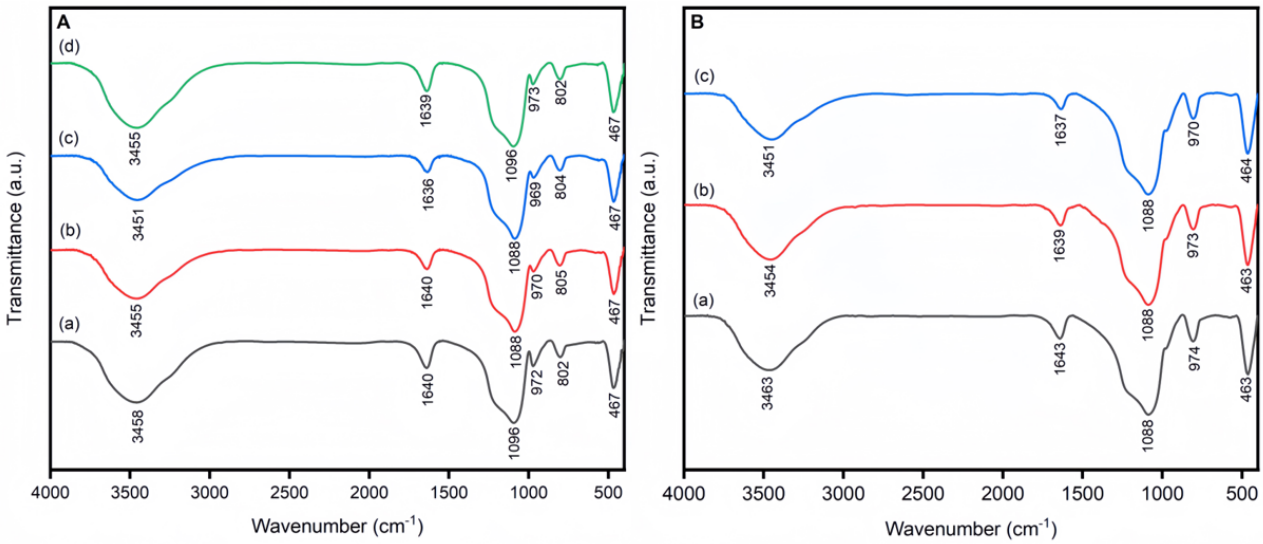


Figure 2. FTIR spectra of SiO2, SMS-1, SMS-1.5, and SMS-2 (A); 1 Ni/SMS-2, 2 Ni/SMS-2, and 3 Ni/SMS-2 (B).

desorption curves presented in Figure 3. $NH_3$–TPD profiles show that pristine $SiO_2$ exhibits only weak ammonia desorption, confirming the presence of very weak acidic sites associated with surface silanol groups. Upon sulfation, the total acidity increases markedly, and higher-temperature desorption features become more pronounced, indicating the generation of stronger acid sites related to sulfate species anchored on the mesoporous silica framework. Increasing sulfate concentration from SMS-1 to SMS-2 results in a corresponding increase in acidity, consistent with the formation of sulfate-derived Brønsted acid sites.

SMS-2 exhibits the highest acidity value, followed by its impregnation with nickel metal (1 Ni/SMS-2, 2 Ni/SMS-2, and 3 Ni/SMS-2). Table 2 indicates that a 1 wt% nickel concentration yields the highest acidity among the concentrations tested. This finding suggests that nickel metal impregnation enhances catalyst acidity, as nickel provides vacant 4p orbitals that serve as Lewis acid sites, accepting electron pairs from other species. However, at 2 wt% and 3 wt% nickel loads, acidity decreases due to excessive metal loading, which results in metal agglomeration outside the material's pores. Both Brønsted and Lewis acid sites contribute to intermediate formation in hydrocracking, so the combination of both acid sites enhances catalyst performance and hydrocracking efficiency.

### 3.3. X-ray Diffractogram Analysis of the Catalysts

The XRD patterns of $SiO_2$, SMS-1, SMS-1.5, and SMS-2 are presented in Figure 4A, while those of 1 Ni/SMS-2, 2 Ni/SMS-2, and 3 Ni/SMS-2 are shown in Figure 4B. The broad peak at $2\theta$ = 22° indicates the amorphous nature of the synthesized silica, consistent across all samples (JCPDS 39-1425). The retention of the broad peak shape suggests that sulfate addition does not

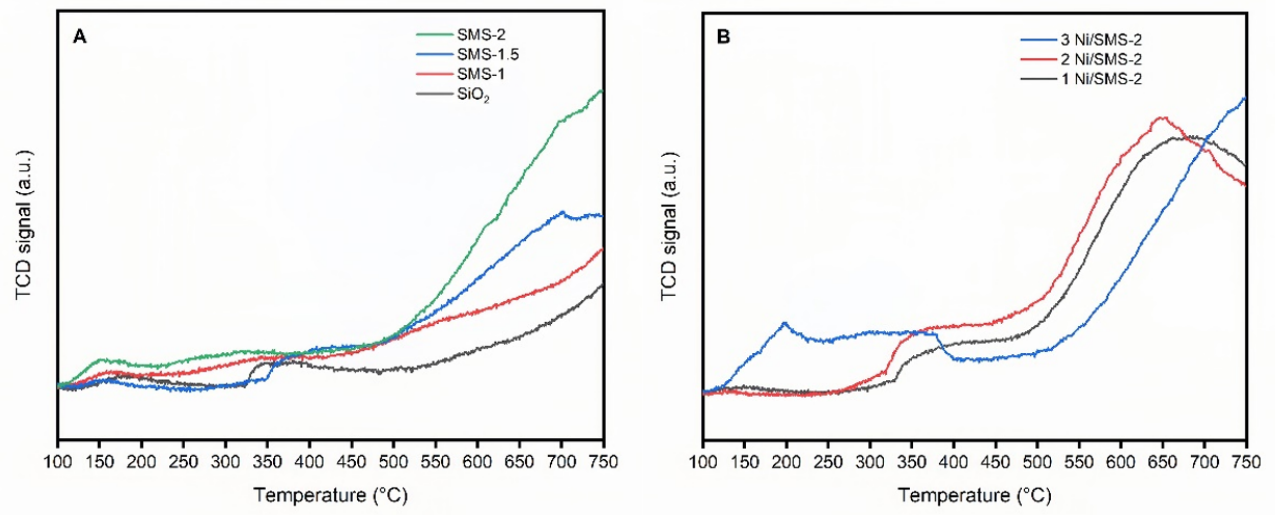


Figure 3. $NH_3$–TPD curves of $SiO_2$, SMS-1, SMS-1.5, and SMS-2 (A); 1 Ni/SMS-2, 2 Ni/SMS-2, and 3 Ni/SMS-2 (B).

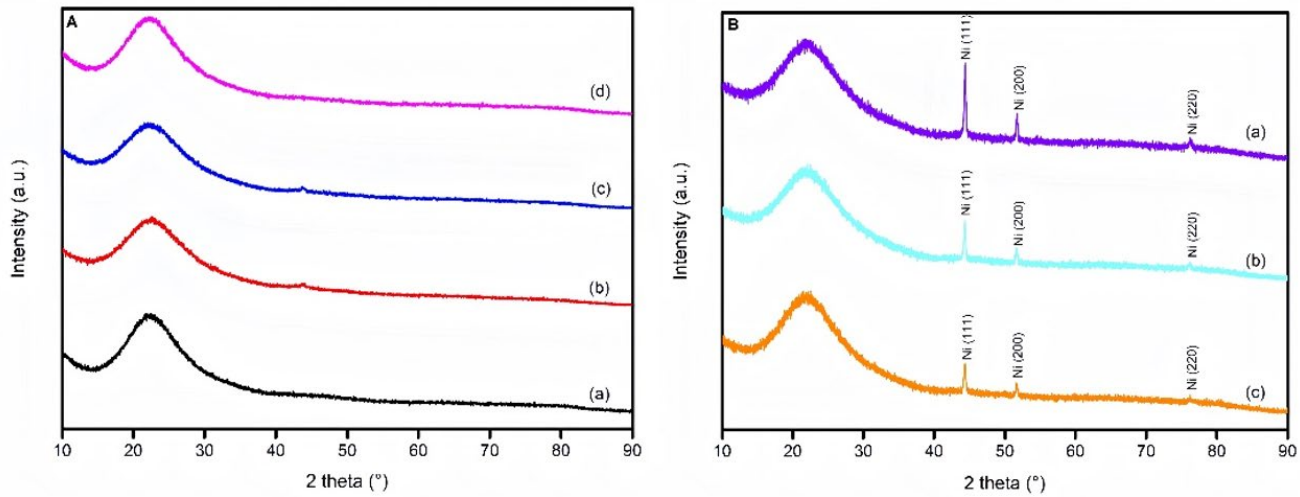


Figure 4. X-ray diffractograms of (a) $SiO_2$, (b) SMS-1, (c) SMS-1.5, and (d) SMS-2 (A); (a) 1 Ni/SMS-2, (b) 2 Ni/SMS-2, and (c) 3 Ni/SMS-2 (B).

affect the catalyst structure. Distinctive peaks for Ni metal impregnated onto the sulfated mesoporous silica are largely identical, indicating that the impregnation technique does not alter the structure of the sulfated mesoporous silica. Nickel nanoparticles with face-centered cubic (fcc) structure display notable peaks at 2θ = 44.51° (111), 51.85° (200), and 76.37° (220) (JCPDS 03–1051) [35], with peak intensity increasing as more metal is impregnated onto the sulfated mesoporous silica. Based on the XRD data, it can be concluded that the crystallite size of Ni increases with higher Ni loading. At low Ni loadings, nickel species are more evenly dispersed across the support surface due to stronger metal–support interactions. At higher loadings, dispersion becomes less effective, leading to the clustering of metal particles and the formation of larger crystallites.

### 3.4. Textural Properties of the Catalysts

The textural properties of all catalysts are summarized in Table 3. The specific surface area was determined using the Brunauer–Emmett–Teller (BET) equation. Incorporation of $NaHCO_3$ as a pore-forming agent released $CO_2$ during calcination, effectively generating silica materials with mesoporous pore diameters. Upon sulfation and subsequent nickel impregnation, both SMS-2 and 1 Ni/SMS-2 exhibited a notable decrease in specific surface area compared to pristine $SiO_2$. This reduction results from partial surface coverage and micropore blockage by sulfate species and nickel particles, as confirmed by the presence of sulfur and nickel in Table 4. The deposition of these species within or near pore openings limits $N_2$ adsorption, leading to a lower measured surface area [36].

Despite the observed decrease in BET surface area, SMS-2 and 1 Ni/SMS-2 exhibit an increase in average pore diameter as determined by BJH pore size distribution analysis. This apparent contradiction can be explained by structural rearrangements occurring during sulfation and subsequent nickel loading. Acidic treatment with $H_2SO_4$ can partially etch the silica framework, leading to wall thinning and the merging of adjacent mesopores, which results in an enlargement of the average pore diameter. Simultaneously, sulfate anchoring and nickel dispersion modify the pore walls and internal surfaces, producing fewer but broader accessible pores.

Consequently, the total pore volume slightly increases after sulfation due to pore expansion, but decreases marginally after nickel impregnation, indicating that nickel species occupy part of the internal voids while preserving the mesoporous structure. These combined effects explain the simultaneous decrease in specific surface area and increase in average pore diameter. Such textural evolution is consistent with previous studies reporting that surface functionalization and metal deposition can induce pore enlargement while reducing the number of accessible adsorption sites, depending on the balance between framework etching and pore blockage.

Figure 5A shows the $N_2$ adsorption–desorption isotherms of $SiO_2$, SMS-2, and 1 Ni/SMS-2. All exhibit type IV isotherms with distinct hysteresis loops, characteristic of mesoporous materials where capillary condensation occurs in mesopores [37]. The

Table 3. Textural properties of the catalysts.

| Catalyst | Specific surface area ($m^2/g$) | Total pore volume ($cm^3/g$) | Average pore diameter (nm) |
|---|---|---|---|
| $SiO_2$ | 699.39 | 0.53 | 3.02 |
| SMS-2 | 528.71 | 0.84 | 6.35 |
| 1 Ni/SMS-2 | 363.55 | 0.60 | 6.61 |

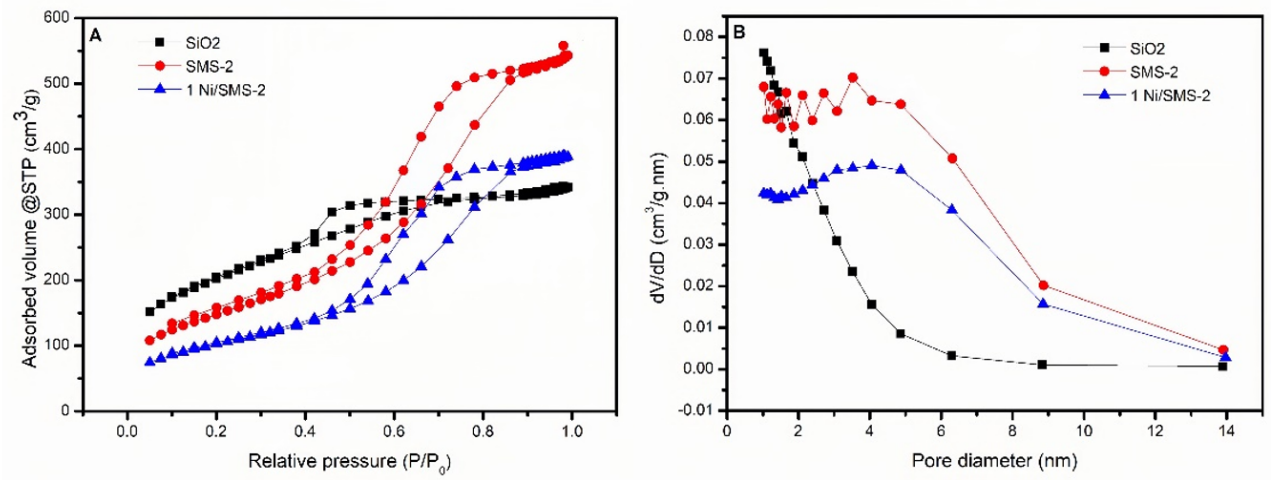


Figure 5. $N_2$ adsorption-desorption isotherm curves (A); Pore diameter distribution curves (B) of the catalysts.

presence of hysteresis confirms mesoporosity but does not necessarily ensure accessibility to large reactant molecules such as triglycerides, since this also depends on pore connectivity, tortuosity, and surface chemistry.

$SiO_2$ displays an H2-type hysteresis loop, typically associated with disordered pores and nonuniform size distributions caused by pore blocking or necking. In contrast, SMS-2 and 1 Ni/SMS-2 exhibit H1-type loops, indicating more uniform cylindrical mesopores with open and interconnected channels [38]. This transformation suggests that sulfation and nickel impregnation influence the silica framework. During sulfation, the acidic medium partially hydrolyzes the siloxane network, leading to wall thinning and pore merging. Subsequent hydrothermal treatment and nickel incorporation promote redeposition of silanol and sulfate species, stabilizing the restructured framework and yielding a more ordered morphology with slightly enlarged channels.

Figure 5B presents the pore size distribution curves obtained from the desorption branch using the Barrett–Joyner–Halenda (BJH) method, following IUPAC recommendations for mesoporous materials due to the metastability of the adsorption branch. The unimodal, narrow distributions with pore sizes mainly between 2 and 14 nm confirm well-defined mesoporosity. The sharp peaks centered at 6–8 nm for SMS-2 and 1 Ni/SMS-2 reflect uniform pore diameters and reduced textural heterogeneity compared with $SiO_2$, which shows a broader distribution indicative of less structural regularity.

The evolution from H2- to H1-type hysteresis, together with the narrower pore size distribution, demonstrates that sulfation and nickel incorporation under hydrothermal conditions not only modify surface chemistry but also reorganize the silica framework, producing a more ordered mesoporous network. Such textural features are beneficial for catalytic applications, ensuring efficient diffusion pathways and maintaining adequate surface area for active-site exposure.

### 3.5. Thermal Stability Analysis of the Catalysts

The thermal stability of $SiO_2$, SMS-2, and 1 Ni/SMS-2 was evaluated by TG/DTA, as shown in Figure 6. The TG curves are expressed as

Table 4. EDX results of the catalysts. (*nd = not detected).

| Catalyst | Elements (wt%) | | | |
|---|---|---|---|---|
| | Si | O | S | Ni |
| $SiO_2$ | 43.89 | 56.11 | nd* | nd* |
| SMS-2 | 31.60 | 67.72 | 0.68 | nd* |
| 1 Ni/SMS-2 | 37.00 | 61.52 | 0.59 | 0.89 |

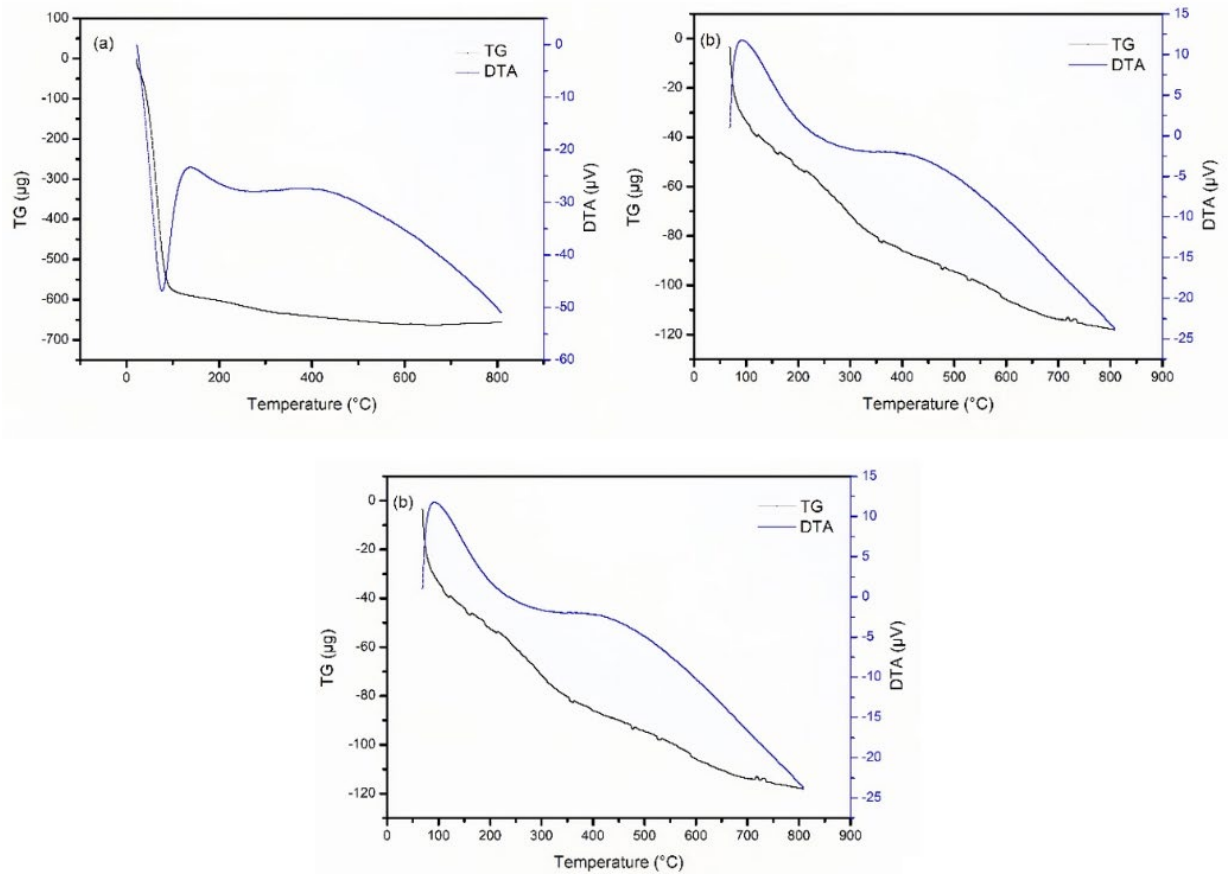


Figure 6. TG/DTA profiles of (a) $SiO_2$, (b) SMS-2, and (c) 1 Ni/SMS-2.

percentage mass loss to ensure valid comparison among samples of different initial weights. Three major weight-loss regions are identified.

The first region (0–110 °C) corresponds to the removal of physically adsorbed water [39]. $SiO_2$ exhibits the highest loss (≈15.44%) compared with SMS-2 (1.05%) and 1 Ni/SMS-2 (0.49%), indicating greater surface hydrophilicity and moisture adsorption. This step produces an endothermic peak at 77 °C, consistent with dehydration (Equation (8)).

$$SiO_2.2H_2O \rightarrow SiO_2 + 2H_2O \quad (8)$$

The second region (110–355 °C) is attributed to the condensation of vicinal silanol groups into siloxane bonds (Si–O–Si). The reduced mass losses of SMS-2 (2.43%) and 1 Ni/SMS-2 (1.49%) compared with $SiO_2$ (16.92%) indicate fewer surface hydroxyls due to sulfation and nickel incorporation, which promote surface densification. The third region (355–625 °C) corresponds to the removal of geminal silanol groups and the thermal decomposition of surface-bound sulfate species. Since free $H_2SO_4$ can not exist above 338 °C, the decomposition involves metal–sulfate or Si–O–$SO_3H$ species releasing $SO_3$ and $O_2$, as detailed in Equations (9) and (10) [40]:

$$–SO_3H(surface) \rightarrow –O(surface) + SO_3 \quad (9)$$
$$SO_3 \rightarrow SO_2 + ½O_2 \quad (10)$$

Endothermic peaks above 400 °C confirm these transformations. The total weight losses of $SiO_2$, SMS-2, and 1 Ni/SMS-2 are 32.36%, 6.72%, and 3.49%, respectively, indicating that sulfation and nickel loading enhance structural integrity and thermal resistance. Overall, surface modification stabilizes the silica framework by reducing hydroxyl content and forming thermally robust sulfate–metal interactions, yielding catalysts with superior high-temperature stability.

### 3.6. Morphological Analysis and Surface Elemental Composition of the Catalysts

Morphological characterization of the catalyst materials was performed using FESEM and TEM. Figure 7 presents FESEM images of $SiO_2$ and catalysts with significant acidity changes due to sulfate addition (SMS-2) and metal loading (1 Ni/SMS-2). The micrographs show that the $SiO_2$ catalyst has a chunk-like morphology with varying sizes, while the addition of sulfate to the support results in an SMS-2 catalyst with an uneven surface and non-uniform particle size, attributed to the agglomeration of $SO_4^{2-}$ ions. This observation is consistent with previous studies indicating that sulfated silica materials produce non-uniform particles and aggregates due to the presence of sulfate ions [41].

As shown in Figure 7, nickel impregnation on sulfated mesoporous silica results in a surface morphology with multiple lumps linked to larger aggregates. Elemental mapping images, provided

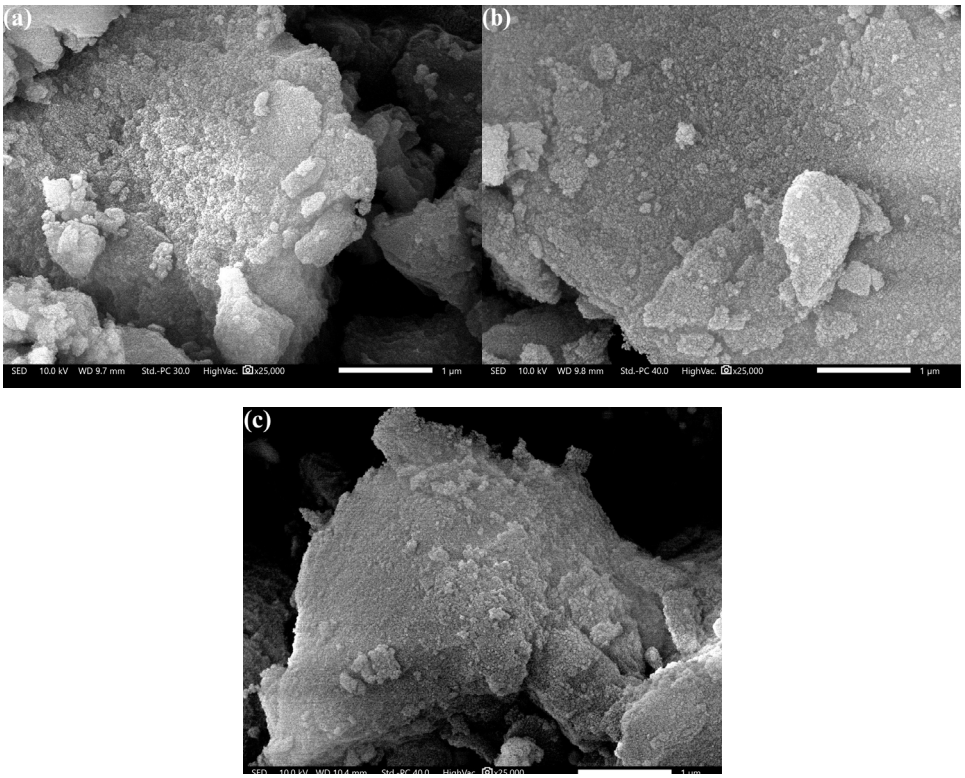


Figure 7. FESEM images at 25,000 times magnification of (a) $SiO_2$, (b) SMS-2, and (c) 1 Ni/SMS-2.

in Figure 8, confirm the presence of sulfur and nickel on the material's surface (see Table 4), demonstrating successful modification of mesoporous silica through sulfuric acid treatment and nickel metal impregnation.

Figure 9 presents TEM images of $SiO_2$, SMS-2, and 1 Ni/SMS-2 materials. All samples consist of aggregated particles rather than isolated individual particles, which limits the direct visualization of mesopores. As a result, pore channels are challenging to discern clearly in the TEM images due to particle overlap and aggregation. Nevertheless, the SMS-2 sample exhibits regions with locally enlarged voids (highlighted by red circles), which qualitatively support the BJH results indicating an increase in average pore diameter after sulfuric acid treatment. This enlargement is attributed to framework modification caused by sulfate incorporation.

In the nickel-impregnated sample, darker contrast regions are observed and can be attributed to nickel species deposited on or within the silica framework, confirming the successful incorporation of nickel. Although TEM does not provide direct evidence of ordered mesoporous channels, the nitrogen adsorption–desorption data demonstrate that mesoporosity is retained. Therefore, BJH/BET and TEM results are complementary: BJH and BET analyses provide statistically averaged textural information, while TEM offers localized structural insight that may not fully capture mesopore ordering in aggregated systems.

### 3.7. Catalytic Activity and Selectivity Assessments

This study examines the catalytic hydrocracking of UCO using $SiO_2$, SMS-2, and 1 Ni/SMS-2. It assesses the effects of acidity modifications through sulfate group and nickel metal additions on the catalytic performance of mesoporous silica catalysts. Before catalytic hydrocracking, thermal hydrocracking (without a catalyst) was conducted at various temperatures to determine the optimum hydrocracking temperature. Table 5 presents the product distribution from thermal hydrocracking at 500, 550, and 600 °C, while Table 6 shows the composition of liquid products. The data indicate that 550 °C is the ideal temperature for hydrocracking in this study, yielding the highest

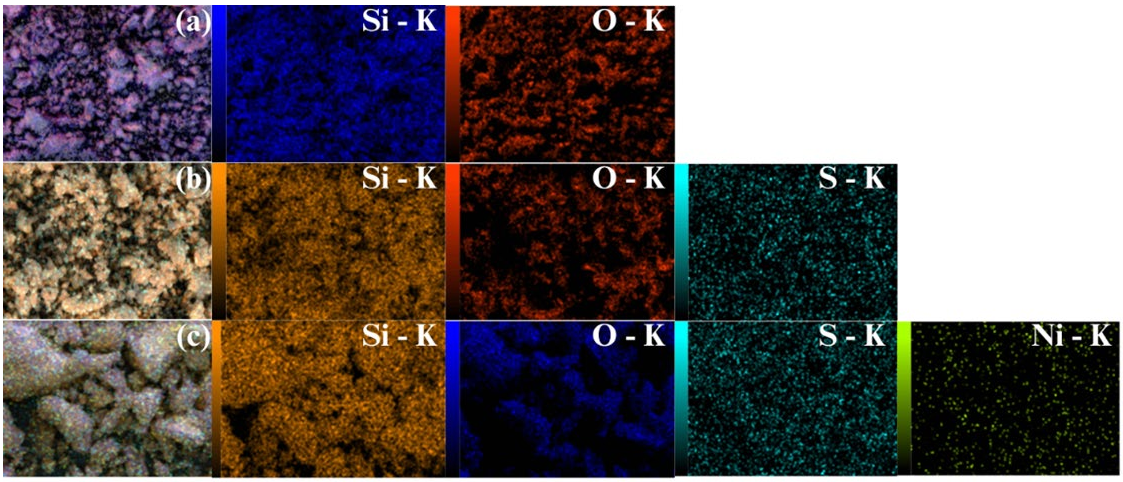


Figure 8. Elemental mapping micrographs of (a) $SiO_2$, (b) SMS-2, and (c) 1 Ni/SMS-2.

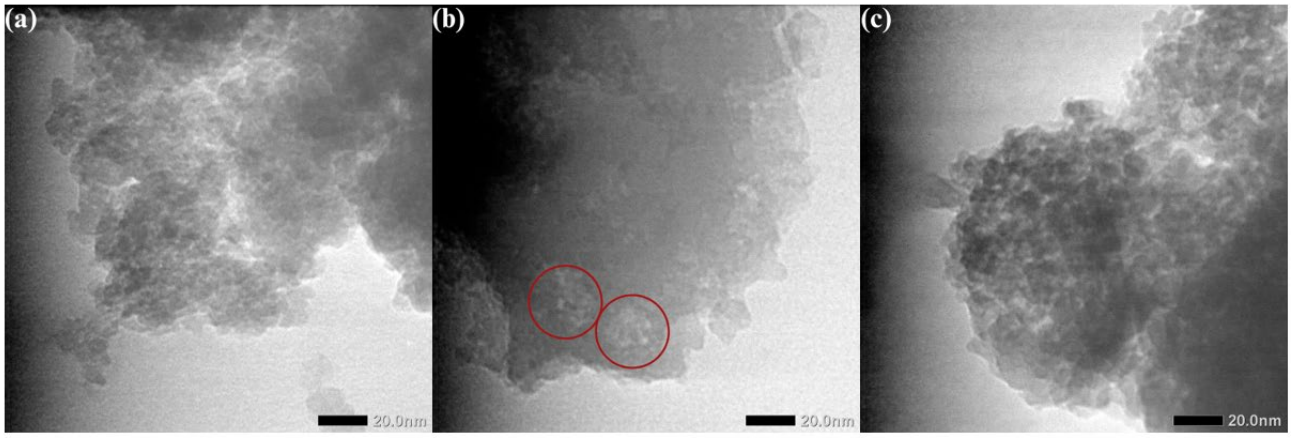


Figure 9. TEM images at 20.0 nm magnification of (a) $SiO_2$, (b) SMS-2, and (c) 1 Ni/SMS-2.

percentage of liquid products and gasoline fractions. Excessively high hydrocracking temperatures lead to increased gas production, indicating a rise in light-fraction hydrocarbons, ultimately reducing the process's efficiency in generating liquid product.

Table 7 summarizes the product conversion percentages from catalytic hydrocracking. The variation in liquid product yield clearly demonstrates the significant influence of catalyst composition on reaction performance. The $SiO_2$ catalyst, with its inherently low surface acidity, produces the lowest liquid yield, reflecting its limited catalytic activity, which refers to the ability of a catalyst to facilitate bond cleavage, hydrogenation, and isomerization reactions that convert triglycerides into smaller hydrocarbon molecules.

The catalytic activity of mesoporous silica is strongly governed by the nature, strength, and distribution of its acidic sites. Pristine mesoporous $SiO_2$ possesses only very weak Brønsted acidity originating from surface silanol (Si–OH) groups, which contributes minimally to hydrocracking activity. Sulfation significantly enhances catalytic performance by introducing sulfate-derived acidic sites that provide sufficient protonic strength to promote C–C bond cleavage reactions. With increasing sulfate loading, the density of effective acid sites increases, facilitating more efficient hydrocracking and explaining the improved catalytic activity observed for SMS-1, SMS-1.5, and SMS-2 compared with pristine $SiO_2$.

Beyond acidity, the mesoporous architecture of the silica support plays a critical role in determining catalytic efficiency. The high surface area and interconnected mesopore network (2–50 nm) enable efficient diffusion of bulky triglyceride molecules to the active sites and promote rapid desorption of lighter hydrocarbon products. This open structure minimizes mass-transfer limitations and suppresses secondary reactions, such as coke formation. Moreover, the inherent thermal and mechanical stability of the silica framework preserves pore accessibility and active-site exposure under hydrocracking conditions, allowing the enhanced acidity introduced by sulfation to be effectively utilized during the reaction.

Among the sulfated catalysts, SMS-2 exhibits the highest acidity. Subsequent nickel impregnation further modifies the acidic properties of the catalyst. As summarized in Table 2, the catalyst containing 1 wt% Ni (1 Ni/SMS-2) shows the highest acidity among the nickel-loaded samples. This enhancement is attributed to the introduction of Lewis acid sites associated with nickel species, which can accept electron pairs through vacant orbitals and thereby complement the existing Brønsted acid sites [42]. However, increasing the nickel loading to 2 wt% and 3 wt% leads to a decrease in acidity, likely due to excessive metal deposition and agglomeration that partially blocks the pores and reduces the accessibility of acidic sites.

Both Brønsted and Lewis acid sites play essential roles in hydrocracking by facilitating the formation of reaction intermediates and promoting C–C bond scission. Therefore, the balanced coexistence of sulfate-derived Brønsted acid sites and nickel-induced Lewis acid sites in 1 Ni/SMS-2 results in enhanced catalytic performance and improved hydrocracking efficiency.

As illustrated in Figure 10, the conversion of UCO begins with the hydrogenolysis of

Table 5. Product conversion of the thermal hydrocracking processes.

| Temperature (°C) | Product conversion (wt%) | |
|---|---|---|
| | Liquid | Gas |
| 500 | 22.30 | 77.70 |
| 550 | 25.00 | 75.00 |
| 600 | 20.80 | 79.20 |

Table 7. Product conversion of the catalytic hydrocracking processes.

| Catalyst | Product conversion (wt%) | | |
|---|---|---|---|
| | Liquid | Gas | Coke |
| $SiO_2$ | 38.10 | 60.63 | 1.27 |
| SMS-2 | 49.20 | 49.59 | 1.21 |
| 1 Ni/SMS-2 (1:100) | 66.10 | 33.29 | 0.61 |
| 1 Ni/SMS-2 (2:100) | 61.70 | 37.24 | 1.06 |
| 1 Ni/SMS-2 (3:100) | 60.80 | 37.83 | 1.37 |

Table 6. Liquid product yield of the thermal hydrocracking processes toward several hydrocarbon fractions. (*determined by GC area of $C_5$–$C_{12}$)

| Temperature (°C) | Gasoline selectivity (%)* | Hydrocarbon yield (wt%) | | | Non-hydrocarbon yield (wt%) | | | |
|---|---|---|---|---|---|---|---|---|
| | | Gasoline | Diesel | Total | Alcohol | Ketone or aldehyde | Fatty acid | Total |
| 500 | 13.63 | 3.04 | 8.96 | 12.00 | 0.00 | 1.18 | 9.12 | 10.30 |
| 550 | 25.60 | 6.40 | 12.40 | 18.80 | 0.18 | 0.51 | 5.51 | 6.20 |
| 600 | 27.79 | 5.78 | 8.39 | 14.17 | 0.23 | 0.65 | 5.75 | 6.63 |

triglycerides into FFAs and glycerol-derived intermediates. The fatty acids subsequently undergo oxygen-removal reactions, including hydrodeoxygenation, hydrodecarbonylation, and hydrodecarboxylation, which involve the cleavage of C–O bonds and lead to the formation of long-chain hydrocarbons. These deoxygenation pathways are accompanied by the evolution of gaseous products such as $H_2O$, CO, and $CO_2$, as schematically indicated in the reaction pathway.

The resulting long-chain hydrocarbons are then converted into gasoline-range hydrocarbons through C–C bond cracking reactions. Sulfate-derived Brønsted acid sites facilitate protonation and the formation of carbonium-ion intermediates, while nickel-associated Lewis acid sites promote the formation of carbenium-ion species, thereby enabling effective C–C bond scission [43]. The synergistic interaction between Brønsted and Lewis acid sites thus enhances hydrocracking efficiency and gasoline-range product formation.

Although gas-phase products are depicted schematically in Figure 10 to illustrate plausible reaction pathways, quantitative analysis of the gas composition was not conducted in this study. Therefore, the relative contributions of hydrodecarbonylation, hydrodecarboxylation, and cracking pathways cannot be distinguished definitively. Nevertheless, the observed liquid product distribution and reduced coke formation on the 1 Ni/SMS-2 catalyst suggest that oxygen-removal and cracking reactions proceed efficiently under the applied conditions. Future work will focus on detailed gas-phase analysis to further elucidate the dominant reaction pathways.

Thermal hydrocracking results in the lowest liquid product yield, indicating that adding a catalyst significantly enhances the hydrocracking process, as evidenced by the higher liquid product conversion. Notably, thermal hydrocracking produces the highest amount of gas products, suggesting that high temperatures in the absence of a catalyst promote irregular chain-breaking reactions through radical mechanisms [44]. The addition of a catalyst enables these high-temperature reactions to proceed more selectively by providing alternative reaction pathways with lower activation energies, allowing a greater proportion of gas-phase hydrocarbons to be converted into liquid products.

Our investigation into the catalyst-to-feed ratio reveals its critical role in hydrocracking. The 1 Ni/SMS-2 catalyst, when used at a 1:100 ratio, demonstrates superior liquid product conversion compared to the 2:100 and 3:100 ratios. This finding emphasizes the importance of carefully controlling catalyst quantities, as excessive catalyst amounts can lead to bulkier particles, reducing the surface area available for reactant-catalyst interaction and thereby diminishing hydrocracking efficiency [45]. As shown in Table 7, too much of the catalyst causes more coke to be formed. This can be caused by the stronger feed sequestration on the catalyst surface, which makes the reaction products challenging to desorb. Later, with the influence of high temperature, carbon deposits will form.

Table 8 presents the yield of each hydrocarbon fraction, including gasoline ($C_5$–$C_{12}$), diesel (> $C_{12}$), and non-hydrocarbon (oxygenated compounds such as fatty acids, ketones or aldehydes, and alcohols). Catalysts with progressively higher acidity enhance selectivity for the gasoline fraction. As shown in Table 8, the

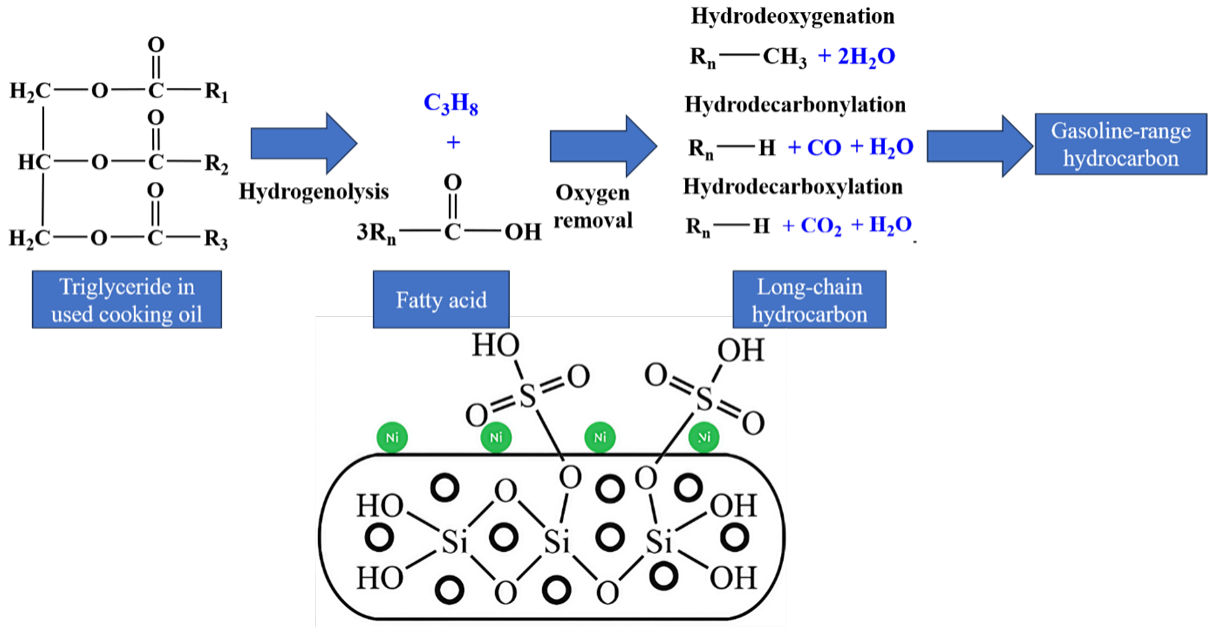


Figure 10. Plausible reaction scheme for the conversion of UCO into biogasoline catalyzed by the 1 Ni/SMS-2 catalyst.

1 Ni/SMS-2 catalyst at a catalyst-to-feed ratio of 1:100 exhibits the highest gasoline yield at 35.47%, followed by diesel at 19.96% and non-hydrocarbons at 10.67%. This is attributed to the presence of sulfate ions and nickel metal, which increase the catalyst's acidity and facilitate the formation of more carbenium and carbonium ions, thereby optimizing the hydrocracking process. However, as the catalyst quantity increases, the gasoline yield of the 1 Ni/SMS-2 catalyst decreases. An excessive amount of catalyst reduces hydrocracking efficiency by yielding more diesel and non-hydrocarbon fractions.

### 3.8. Liquid Product Evaluation

Figure 11 illustrates the hydrocarbon range within the gasoline fraction in the liquid products from hydrocracking compared to commercial gasoline. Neither hydrocracking products nor commercial gasoline contains hydrocarbon chains with five or six carbon atoms. Our biogasoline and commercial gasoline present hydrocarbons ranging from $C_7$ to $C_{12}$. Hydrocarbons with eleven carbon atoms dominate our biogasoline, whereas commercial gasoline primarily consists of nine-carbon hydrocarbons. Olefins are the primary compounds in our biogasoline, while commercial gasoline mainly contains aromatics. This discrepancy is due to the atmospheric pressure used in the hydrocracking process, limiting optimal hydrogenation and aromatization, which leads to a predominance of olefin compounds in the biogasoline [46]. Additionally, the abundance of olefins in our hydrocracking products may result from a penta-coordinated carbonium ion mechanism, which requires further hydrogenation to form paraffins.

This outcome is an advantage of this research, as our biogasoline, lacking aromatics, can provide cleaner combustion than commercial gasoline, which has a high aromatic content. The legislative body limits the amount of aromatics allowed in fuel. This is primarily because high levels of aromatics in fuel lead to increased emissions of unburned hydrocarbons, such as carbon monoxide and aromatic compounds like benzene, into the atmosphere [47]. However, the octane number produced from olefin combustion is relatively low compared to aromatics, indicating the need for further studies to improve biogasoline quality.

The calorific value test, conducted using a bomb calorimeter, is essential to measure the energy content of fuels, specifically their heat release during combustion, which is critical for determining fuel quality and performance. Table 9 compares the test results of our biogasoline with commercial gasoline. Biogasoline has a calorific value higher than commercial gasoline, although

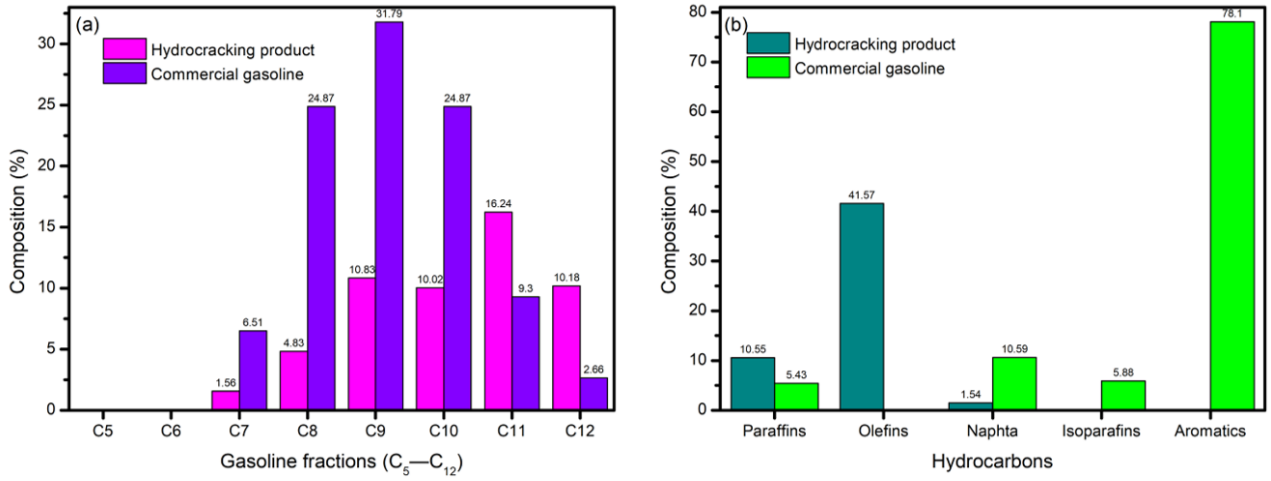


Figure 11. (a) Hydrocarbon chain range and (b) hydrocarbon composition comparison between liquid product from hydrocracking of UCO using the 1 Ni/SMS-2 catalyst and commercial gasoline.

Table 8. Liquid product yield of the catalytic hydrocracking processes toward several hydrocarbon fractions. (*determined by GC area of $C_5$–$C_{12}$).

| Catalyst | Gasoline selectivity (%)* | Hydrocarbon yield (wt%) | | | Non-hydrocarbon yield (wt%) | | | |
|---|---|---|---|---|---|---|---|---|
| | | Gasoline | Diesel | Total | Alcohol | Ketone or aldehyde | Carboxylic acid | Total |
| $SiO_2$ | 22.05 | 8.40 | 18.35 | 26.75 | 0.19 | 2.43 | 8.73 | 11.35 |
| SMS-2 | 33.27 | 16.37 | 29.01 | 45.38 | 0.00 | 0.00 | 3.82 | 3.82 |
| 1 Ni/SMS-2 (1:100) | 53.66 | 35.47 | 21.96 | 57.43 | 2.29 | 4.48 | 1.90 | 8.67 |
| 1 Ni/SMS-2 (2:100) | 40.34 | 24.89 | 25.94 | 50.83 | 2.13 | 5.80 | 2.94 | 10.87 |
| 1 Ni/SMS-2 (3:100) | 17.40 | 10.58 | 39.25 | 49.83 | 1.85 | 5.02 | 4.10 | 10.97 |

the difference is not substantial. Thus, our biogasoline is comparable to commercial gasoline in terms of energy content. A fuel's calorific value is an essential measure of its effectiveness for energy production. Generally, fuels with higher calorific values are considered better because they release more energy per unit of weight or volume when burned [48]. When the products cool to the initial sample temperature, a higher calorific value indicates that all of the heat generated from fuel combustion is being detected [49]. This means less fuel is needed to produce the same amount of energy, making it more efficient and cost-effective. The significance of the calorific value obtained can not be overstated. In future studies, evaluating additional fuel specifications such as flash point, boiling point, density, kinematic viscosity, octane number, and oxidation stability will be necessary. This will help enhance confidence in the potential application of this biogasoline in real vehicle engines.

FTIR analysis was also performed to compare functional groups between the feed and hydrocracking products. The FTIR spectra in Figure 12 show a reduction in the peak around 1700 $cm^{-1}$, indicating a decrease in C=O groups. This confirms that the biogasoline contain fewer oxygenated compounds. The reduction in oxygen content is also evident from significant changes in absorption peaks around 1000–1250 $cm^{-1}$, representing C–O groups [50]. The results can be explained by how triglyceride and fatty acid molecules undergo carbon–oxygen bond-breaking before the C–C bond-breaking stage.

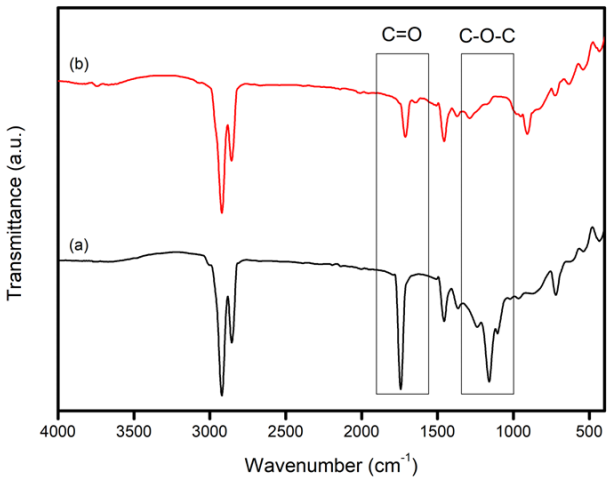


Figure 12. FTIR spectra of (a) UCO feed and (b) liquid product from hydrocracking of UCO using

Table 9. Calorific value test results.

| Sample | Calorific value (MJ/kg) |
|---|---|
| Biogasoline | 42.63 |
| Commercial gasoline | 41.90 |

3.9. Reusability of the 1 Ni/SMS-2 Catalyst

The 1 Ni/SMS-2 catalyst, which demonstrated the highest liquid product conversion and gasoline yield at a catalyst-to-feed ratio of 1:100, was evaluated for reusability over three cycles. Table 10 presents the results of the product conversion tests for the reused 1 Ni/SMS-2 catalyst. The decrease in liquid product conversion was accompanied by a reduction in the gasoline yield, as illustrated in Table 11. These findings suggest that the catalyst's performance deteriorates with increased usage. The decrease in catalyst performance can be attributed to factors such as sintering and deactivation due to coke production.

The results from FESEM–EDX Mapping and TEM characterization support this observation. Figure 13 displays the FESEM–EDX Mapping and TEM morphological images of the spent Ni 1/SMS-2 catalyst. After three uses, the morphology of the spent Ni 1/SMS-2 catalyst indicates sintering phenomena, which is evidenced by the aggregation of materials. Following the reusability tests, the catalyst also experienced deactivation due to coke deposition, as shown by the presence of carbon in Table 12.

Coke blockage of catalyst active sites is common when heterogeneous catalysts are used for biofuel production. According to Zhou *et al.* [51], coke can be regenerated through at least three methods: hydrogenation, oxidation, and gasification. Each technique offers its advantages for coke removal. However, from a sustainability perspective, the gasification method using $CO_2$ as a mild oxidizing agent is an up-and-coming option today. Through the Reverse Boudouard (RB) reaction, the coke on the catalyst surface reacts with $CO_2$, which helps improve carbon balance [52]. The findings of this work provide significant opportunities for other researchers to explore this method further to reduce catalyst deactivation.

Table 12. Elemental composition of the spent Ni 1/SMS-2 catalyst obtained by EDX. (*nd = not detected)

| Elements (wt %) | | | | |
|---|---|---|---|---|
| Si | O | S | Ni | C |
| 17.55 | 48.71 | nd* | 0.77 | 32.97 |

Table 10. Product conversion results from reusability test of the 1 Ni/SMS-2 catalyst.

| Usage | Product conversion (wt%) | | |
|---|---|---|---|
| | Liquid | Gas | Coke |
| 1 (*fresh*) | 66.10 | 33.90 | 0.61 |
| 2 | 65.70 | 33.49 | 0.81 |
| 3 | 60.60 | 38.12 | 1.28 |

3.10. Comparison Results Between the Present Work with Some Previous Studies

Table 13 provides information about previous research on biogasoline production. Our research findings indicate that nickel metal, as an active metal on sulfated mesoporous silica support, achieves superior results in producing biogasoline from catalytic hydrocracking of UCO compared to chromium metal [39]. Moreover, this study demonstrates improvement over the work of Rambabu *et al*. [53], who conducted hydroprocessing of date palm seed oil over a tantalum phosphate catalyst at 10 bar $H_2$ pressure, achieving 35.90% biogasoline. Furthermore, our findings compare favorably to those of Ibrahim *et al*. [54], who used a high-pressure reactor to convert waste palm oil to biogasoline. Conducting the hydrocracking process at atmospheric pressure is an advantage of our research, as it reduces energy consumption and aligns with the Sustainable Development Goals. Additionally, our study used only Ni metal, which is cheaper and more abundant in Indonesia. Therefore, this catalyst could be a promising candidate for green industrial biofuel production in the future.

In another report, Hasanudin and co-workers [55] researched the hydrocracking of crude palm oil with bentonite-ZrN catalyst, producing 21.21% biogasoline. Another study by Widyastuti *et al.* [56] reported using crude palm oil as feedstock for biogasoline production. Additionally, research by Aulia and co-workers [57] indicated using fresh palm oil as a feedstock. Since crude palm oil can still be used as raw material for derivative products for human consumption, selecting UCO as feedstock is better to support sustainability and environmental balance. Consequently, further optimization of hydrocracking parameters is essential to achieve higher liquid product conversion and gasoline yield, along with studies on catalyst reproducibility. Additional analysis, including life-cycle and techno-economic assessments, is required to evaluate the biogasoline production method against existing fossil-based gasoline production methods.

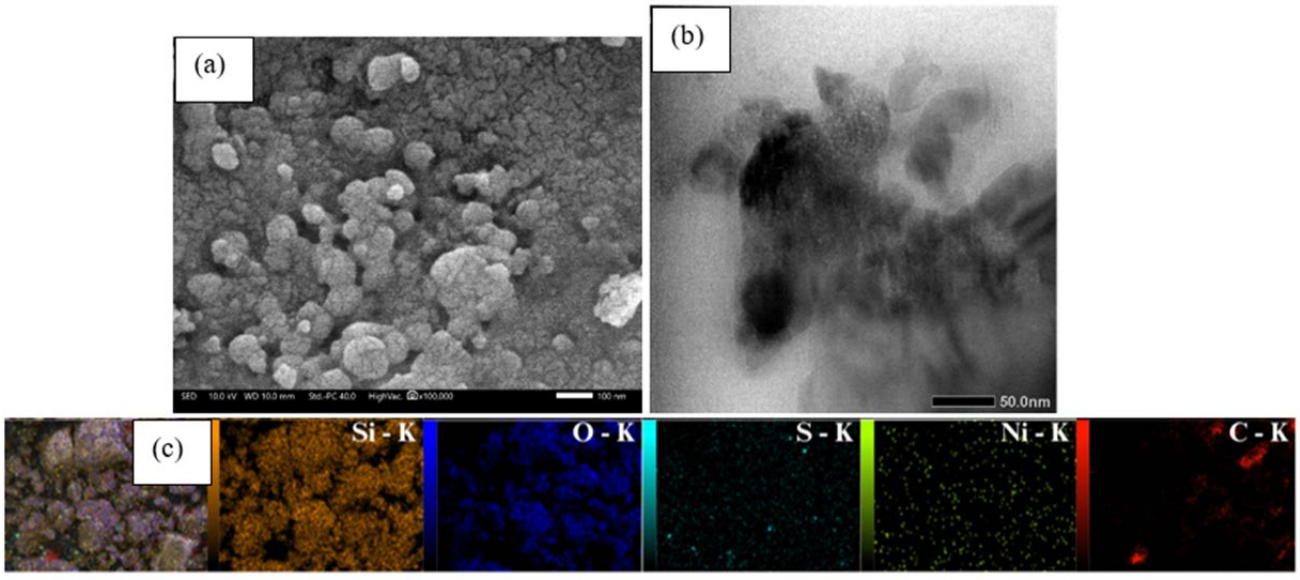


Figure 13. (a) FESEM, (b) TEM, and (c) elemental mapping images of the spent Ni 1/SMS-2 catalyst.

Table 11. Liquid product yield from reusability test of the 1 Ni/SMS-2 catalyst. (*determined by GC area of $C_5$–$C_{12}$).

| Usage | Gasoline selectivity (%)* | Hydrocarbon yield (wt%) | | | Non-hydrocarbon yield (wt%) | | | |
|---|---|---|---|---|---|---|---|---|
| | | Gasoline | Diesel | Total | Alcohol | Ketone or aldehyde | Carboxylic acid | Total |
| 1 (*fresh*) | 53.66 | 35.47 | 21.96 | 57.43 | 2.29 | 4.48 | 1.90 | 8.67 |
| 2 | 47.05 | 30.91 | 26.84 | 57.75 | 2.19 | 3.82 | 1.94 | 7.95 |
| 3 | 45.79 | 27.75 | 25.13 | 52.88 | 1.70 | 3.62 | 2.40 | 7.72 |

## 4. Conclusion

In summary, mesoporous silica was successfully synthesized using sodium bicarbonate as a pore-directing agent, followed by treatment with 2 M $H_2SO_4$ and 1 wt% nickel metal impregnation via the hydrothermal method. This produced the 1 Ni/SMS-2 catalyst, which demonstrated the highest acidity compared to variations in sulfuric acid concentration and nickel loading. The enhanced acidity of the 1 Ni/SMS-2 catalyst resulted in superior activity and selectivity, achieving a liquid product conversion of 66.10% and a gasoline fraction of 35.47% relative to SMS-2 and $SiO_2$. Sulfuric acid modification and nickel addition effectively improved the catalytic performance of mesoporous silica for biogasoline production. Nonetheless, further research is warranted to maximize liquid product conversion and gasoline yield by optimizing the hydrocracking parameters, such as reaction time and hydrogen supply, for its practical scalability. In addition, fractional distillation must be considered in the next work to separate the non-gasoline fraction. Thus, the properties can be more matched with commercial gasoline.

The obtained biogasoline, with a calorific value of 42.63 MJ/kg, closely matches that of commercial gasoline (41.90 MJ/kg). As technological progress and the demand for sustainable energy alternatives continue, biogasoline production from UCO offers promising potential, supporting circular economy initiatives and strengthening energy security. Collectively, this study presents a safer approach to biogasoline production via catalytic hydrocracking at atmospheric pressure, yielding hydrocarbon products devoid of aromatics, which contributes to cleaner combustion and reduced carbon footprint for a more sustainable future.

## Acknowledgment

The authors would like to express their gratitude to the National Research and Innovation Agency (BRIN) Indonesia and Indonesia Endowment Fund for Education Agency (LPDP) for funding this work through *Riset dan Inovasi untuk Indonesia Maju* (RIIM) Batch III 2023 Project with Contract Number 30/IV/KS/05/2023 and 2243/UN1/DITLIT/Dit-Lit/PT.01.03/2023 (second year project based on B-1241/II.7.5/FR.00.03/2/2025). The authors also acknowledge the facilities and scientific support from the Physical Chemistry Laboratory, Department of Chemistry, Universitas Gadjah Mada, the Advanced Characterization Laboratories Serpong and the Advanced Physics Imaging Laboratories Serpong, the National Research and Innovation Agency (BRIN) Indonesia through E-Layanan Sains.

## CRedit Author Statement

Author Contributions: K. Wijaya: Conceptualization, Formal analysis, Funding acquisition, Project administration, Resources, Supervision, Validation, Writing – original draft. M.F. Vebryana: Data curation, Investigation, Software, Visualization, Writing – original draft. N. Prasetyo: Formal analysis, Supervision, Validation, Writing – review & editing. A.J. Saviola: Conceptualization, Methodology, Visualization, Writing – review & editing. W.D. Saputri: Formal analysis, Supervision, Validation, Writing – review & editing. A.K. Amin: Formal analysis, Supervision, Validation, Writing – review & editing. L. Hauli: Formal analysis, Supervision, Validation, Writing – review & editing. S. Gea: Formal analysis, Supervision, Validation, Writing – review & editing. All authors have read and agreed to the published version of the manuscript.

Table 13. Comparison between the present work with other studies on biogasoline production.

| Feedstock | Catalyst | Operational conditions | Obtained biogasoline (%) | Ref. |
|---|---|---|---|---|
| Coconut oil | Ni-BZS 0.5 | T = 450 °C, t = 1 h, P = 1 atm, reactor type = microreactor | 30.52 | [26] |
| Waste frying oil | $Ni_2Mo_2$/HS3 | T = 475 °C, t = 2 h, P = atm, reactor type = fixed-bed reactor | 18.64 | [30] |
| Used cooking oil | Cr-SS 1 | T = 450 °C, t = 2 h, P = 1 atm, reactor type = semi-batch reactor | 29.38 | [39] |
| Date palm seed oil | TaPa | T = 400 °C, t = 3 h, P = 9.87 atm, reactor type = batch reactor | 35.90 | [53] |
| Waste cooking oil | $CoAl_2O_4$ | T = 400 °C, t = 1 h, P = 70 bar, reactor type = continuous high-pressure reactor | 24.00 | [54] |
| Crude palm oil | Bentonite-ZrN | T = 450 °C, t = 0.12 h, P = 1 atm, reactor type = semi-batch reactor | 21.21 | [55] |
| Crude palm oil | HZSM-5 | T = 400 °C, t = 4 h, P = not stated, reactor type = not stated | 39.56 | [56] |
| Palm oil | Z/CNC-4 | T = 550 °C, t = 4 h, P 1 atm, reactor type = fixed-bed reactor | 30.30 | [57] |
| Used cooking oil | 1 Ni/SMS-2 | T = 550 °C, t = 2 h, P = 1 atm, reactor type = semi-batch reactor | 35.47 | Present work |

## References


[1] Yolcan, O.O. (2023). World energy outlook and state of renewable energy: 10-year evaluation. *Innovation and Green Development*, 2, 100070. DOI: 10.1016/j.igd.2023.100070.

[2] Sari, E.G., Sofwan, M. (2021). Carbon dioxide ($CO_2$) emissions due to motor vehicle movements in Pekanbaru City, Indonesia. *Journal of Geoscience, Engineering, Environment, and Technology*, 6, 234–242. DOI: 10.25299/jgeet.2021.6.4.7692.

[3] Perdana, B.E.G. (2021). Circular economy of used cooking oil in Indonesia: Current practices and development in Special Region of Yogyakarta. *Journal of World Trade Studies*, 6, 28–39. DOI: 10.22146/jwts.v6i1.1541.

[4] Lam, S.S., Mahari, W.A.W., Cheng, C.K., Omar, R., Chong, C.T., Chase, H.A. (2016). Recovery of diesel-like fuel from waste palm oil by pyrolysis using a microwave heated bed of activated carbon. *Energy*, 115, 791–799. DOI: 10.1016/j.energy.2016.09.076.

[5] Meller, E., Gutkin, V., Aizenshtat, Z., Sasson, Y. (2016). Catalytic hydrocracking–hydrogenation of castor oil fatty acid methyl esters over nickel substituted polyoxometalate catalyst. *ChemistrySelect*, 1, 6396–6405. DOI: 10.1002/slct.201601030.

[6] de la Osa, A.R., Sánchez, P., Dorado, F., García-Vargas, J.M. (2019). Silica-based catalysts for fuel applications. *Chemistry of Silica and Zeolite-Based Materials*, 2019, 143–161. DOI: 10.1016/B978-0-12-817813-3.00008-0.

[7] Motokura, K., Ding, S., Usui, K., Kong, Y. (2021). Correction to enhanced catalysis based on the surface environment of the silica-supported metal complex. *ACS Catalysis*, 11, 14302–14302. DOI: 10.1021/acscatal.1c04934.

[8] Hassan, M.A., Wang, W., Dong, B., Anwar, H., Chang, Z., Wei, D., Khan, K. (2024). Production of biodiesel from waste culinary oil catalyzed by $S_2O_8^{2-}/TiO_2–SiO_2$ solid superacid catalyst prepared with recovered $TiO_2$ from spent SCR. *Materials Today Sustainability*, 26, 100730. DOI: 10.1016/j.mtsust.2024.100730.

[9] Carvalho, G.C., Marena, G.D., Karnopp, J.C.F., Jorge, J., Sábio, R.M., Martines, M.A.U., Bauab, T.M., Chorilli, M. (2022). Cetyltrimethylammonium bromide in the synthesis of mesoporous silica nanoparticles: General aspects and in vitro toxicity. *Advances in Colloid and Interface Science*, 307, 102746. DOI: 10.1016/j.cis.2022.102746.

[10] Tang, M., Zhang, P., Liu, J., Long, Y., Cheng, Y., Zheng, H. (2020). Cetyltrimethylammonium chloride-loaded mesoporous silica nanoparticles as a mitochondrion-targeting agent for tumor therapy. *RSC Advances*, 10, 17050–17057. DOI: 10.1039/D0RA02023K.

[11] Eremina, A.S., Kargina, Y.V., Kharin, A.Y., Petukhov, D.I., Timoshenko, V.Y. (2022). Mesoporous silicon nanoparticles covered with PEG molecules by mechanical grinding in aqueous suspensions. *Microporous and Mesoporous Materials*, 331, 111641. DOI: 10.1016/j.micromeso.2021.111641.

[12] Hossain, M.S., Shenashen, M.A., Awual, M.E., Rehan, A.I., Rasee, A.I., Waliullah, R.M., Kubra, K.T., Salman, M.S., Sheikh, M.C., Hasan, M.N., Hasan, M.M., Islam, A., Khaleque, M.A., Marwani, H.M., Alzahrani, K.A., Asiri, A.M., Rahman, M.M., Awual, Md.R. (2024). Benign separation, adsorption, and recovery of rare-earth Yb(III) ions with specific ligand-based composite adsorbent. *Process Safety and Environmental Protection*, 185, 367–374. DOI: 10.1016/j.psep.2024.03.026.

[13] Zhang, W., Wang, Z., Huang, J., Jiang, Y. (2021). Zirconia-based solid acid catalysts for biomass conversion. *Energy & Fuels*, 35, 9209–9227. DOI: 10.1021/acs.energyfuels.1c00709.

[14] Delarmelina, M., Deshmukh, G., Goguet, A., Catlow, C.R.A., Manyar, H. (2021). Role of sulfation of zirconia catalysts in vapor phase ketonization of acetic acid. *The Journal of Physical Chemistry C*, 125, 27578–27595. DOI: 10.1021/acs.jpcc.1c06920.

[15] Zhao, M., Wei, X., Zong, Z. (2016). Preparation of a new solid acid and its catalytic performance in di(1-naphthyl)methane hydrocracking. *Chinese Journal of Catalysis*, 37, 1324–1330. DOI: 10.1016/s1872-2067(15)61112-3.

[16] Padalkar, K., Phatangare, S., Takale, R., Pisal, A., Chaskar. (2015). Silica supported sodium hydrogen sulfate and Indion 190 resin: Efficient heterogeneous catalysts for facile synthesis of bis-(4-hydroxycoumarin-3-yl)methanes. *Journal of the Saudi Chemical Society*, 19, 42–45. DOI: 10.1016/j.jscs.2011.12.015.

[17] Herlina, I., Simanjuntak, W., Rilyanti, M., Safitra, E.R. (2019). Physical characteristics and catalytic activity of sulfated sugarcane bagasse silica ($SiO_2/SO_3H^+$) for coconut oil transesterification. *Rasayan Journal of Chemistry*, 12, 1595–1600. DOI: 10.31788/RJC.2019.1235170.

[18] Fadilah, C., Kurniawan, C., Ridwan, M., Muttaqqi, M.A., Agustian, E., Andreani, A.S., Dwiatmoko, A.A., Yati, I. (2023). Synthesis of superacid sulfated $TiO_2$ nanowires for esterification of waste cooking oil. *Reaction Kinetics, Mechanisms and Catalysis*, 136, 1529–1544. DOI: 10.1007/s11144-023-02401-3.

[19] Saab, R., Damaskinos, C.M., Polychronopoulou, K., Efstathiou, A.M., Charisiou, N., Goula, M., Hinder, S.J., Baker, M.A., Schiffer, A. (2022). Ni/CNT/Zeolite-Y composite catalyst for efficient heptane hydrocracking: Steady-state and transient kinetic studies. *Applied Catalysis A: General*, 630, 118437. DOI: 10.1016/j.apcata.2021.118437.

[20] García-Pérez, D., Lopez-Garcia, A., Reñones, P., Alvarez-Galvan, M.C., Campos-Martin, J.M. (2022). Influence of nickel loading on the hydroisomerization of n-dodecane with nickel–tungsten oxide–alumina supported catalysts. *Molecular Catalysis*, 529, 112556. DOI: 10.1016/j.mcat.2022.112556.

[21] Ding, F., Zhang, Y., Yuan, G., Wang, K., Dragutan, I., Dragutan, V., Cui, Y., Wu, J. (2015). Synthesis and catalytic performance of $Ni/SiO_2$ for hydrogenation of 2-methylfuran to 2-methyltetrahydrofuran. *Journal of Nanotechnology*, 2015, 791529. DOI: 10.1155/2015/791529.

[22] Hongloi, N., Prapainainar, P., Seubsai, A., Sudsakorn, K., Prapainainar, C. (2019). Nickel catalysts with different supports for green diesel production. *Energy*, 182, 306–320. DOI: 10.1016/j.energy.2019.06.020.

[23] Hamid, A.-H., Ali, L., Shittu, T., Kuttiyathil, M.S., Ismail, O., Khaleel, A., Altarawneh, M. (2023). Transformation of levoglucosan into liquid fuel via catalytic upgrading over $Ni–CeO_2$ catalysts. *Molecular Catalysis*, 547, 113382. DOI: 10.1016/j.mcat.2023.113382.

[24] Hongloi, N., Rahman, T., Biswas, B., Feyzbar-Khalkhali-Nejad, F., Prapainainar, C., Wongsurakul, P., Ivanchenko, P., Jaisi, D.P., Aransiola, E., Zhang, L., Ammar, M., Baltrusaitis, J., Prapainainar, P., Adhikari, S. (2024). Biofuel production from palm oil deoxygenation using nickel–molybdenum on zirconia catalyst with glycerol as a hydrogen donor. *Energy Conversion and Management: X*, 24, 100781. DOI: 10.1016/j.ecmx.2024.100781.

[25] Wijaya, K., Kurniawan, M.A., Saputri, W.D., Trisunaryanti, W., Mirzan, M., Hariani, P.L., Tikoalu, A.D. (2021). Synthesis of nickel catalyst supported on $ZrO_2/SO_4^{2-}$ pillared bentonite and its application for conversion of coconut oil into gasoline via hydrocracking process. *Journal of Environmental Chemical Engineering*, 9, 105399. DOI: 10.1016/j.jece.2021.105399.

[26] Riyandi, R., Rinaldi, N., Yunarti, R.T., Dwiatmoko, A.A., Simanjuntak, F.S.H. (2024). Effect of various silica-supported nickel catalysts on the production of bio-hydrocarbons from oleic acid. *International Journal of Renewable Energy Development*, 13, 601–607. DOI: 10.61435/ijred.2024.60054.

[27] Wang, H., Wu, Y., He, L., Liu, Z. (2012). Supporting tungsten oxide on zirconia by hydrothermal and impregnation methods and its use as a catalyst to reduce the viscosity of heavy crude oil. *Energy & Fuels*, 26, 6518–6527. DOI: 10.1021/ef301064b.

[28] Leangtanom, P., Wisitsoraat, A., Tuantranont, A., Chanlek, N., Pookmanee, P., Satienperakul, S., Phanichphant, S., Kruefu, V. (2023). Microwave-assisted hydrothermal/impregnation synthesis of $Cu_2O$-decorated $rGO/In_2O_3$ nanorices for sensitive $SO_2$ gas sensors. *ACS Applied Nano Materials*, 6, 12980–12990. DOI: 10.1021/acsanm.3c01712.

[29] Kumar, A., Reddy, S.N. (2022). Hydrothermal treatment of metal-impregnated biomass for the generation of $H_2$ and nanometal–carbon hybrids. *Environmental Research*, 205, 112536. DOI: 10.1016/j.envres.2021.112536.

[30] Nadia, A., Wijaya, K., Falah, I.I., Sudiono, S., Budiman, A. (2022). Self-regeneration of monodisperse hierarchical porous NiMo/silica catalyst induced by $NaHCO_3$ for biofuel production. *Waste and Biomass Valorization*, 13, 2335–2347. DOI: 10.1007/s12649-021-01634-4.

[31] Pratika, R.A., Wijaya, K., Utami, M., Mulijani, S., Patah, A., Alarifi, S., Mani, R.R., Yadav, K.K., Ravindran, B., Chung, W.J., Chang, S.W., Munusamy-Ramanujam, G. (2023). The potency of hydrothermally prepared sulfated silica ($SO_4/SiO_2$) as a heterogeneous acid catalyst for ethanol dehydration into diethyl ether. *Chemosphere*, 341, 139822. DOI: 10.1016/j.chemosphere.2023.139822.

[32] Ellerbrock, R., Stein, M., Schaller, J. (2022). Comparing amorphous silica, short-range-ordered silicates and silicic acid species by FTIR. *Scientific Reports*, 12, 11708. DOI: 10.1038/s41598-022-15882-4.

[33] Monsur, H.A., Jaswir, I., Simsek, S., Amid, A., Alam, Z. (2017). Chemical structure of sulfated polysaccharides from brown seaweed (*Turbinaria turbinata*). *International Journal of Food Properties*, 20, 1457–1469. DOI: 10.1080/10942912.2016.1211144.

[34] Sabilladin, A., Saviola, A.J., Wijaya, K., Hutama, A.S., Pradipta, M.F., Saputri, W.D., Ismail, H., Budhijanto, B., Oh, W.-C., Ravindran, B. (2024). Optimizing nitrobenzene synthesis catalyzed by sulfated silica ($SO_4/SiO_2$) through response surface methodological approach. *Korean Journal of Materials Research*, 34, 341–354. DOI: 10.3740/MRSK.2024.34.7.341.

[35] Davar, F., Fereshteh, Z., Salavati-Niasari, M. (2009). Nanoparticles Ni and NiO: Synthesis, characterization and magnetic properties. *Journal of Alloys and Compounds*, 476, 797–801. DOI: 10.1016/j.jallcom.2008.09.121.

[36] Amin, M.H. (2020). Relationship between the pore structure of mesoporous silica supports and the activity of nickel nanocatalysts in the $CO_2$ reforming of methane. *Catalysts*, 10, 51. DOI: 10.3390/catal10010051.

[37] Thommes, M., Kaneko, K., Neimark, A.V., Olivier, J.P., Rodriguez-Reinoso, F., Rouquerol, J., Sing, K.S.W. (2015). Physisorption of gases, with special reference to the evaluation of surface area and pore size distribution (IUPAC Technical Report). *Pure and Applied Chemistry*, 87, 1051–1069. DOI: 10.1515/pac-2014-1117.

[38] Calzaferri, G., Gallagher, S.H., Lustenberger, S., Walther, F., Brühwiler, D. (2023). Multiple equilibria description of type H1 hysteresis in gas sorption isotherms of mesoporous materials. *Materials Chemistry and Physics*, 296, 127121. DOI: 10.1016/j.matchemphys.2022.127121.

[39] Wijaya, K., Ningrum, T.S., Saviola, A.J., Prasetyo, N., Ardelia, Z.L., Fitria, R.A., Gea, S., Hauli, L., Amin, A.K., Saputri, W.D., Setiawan, A., Oh, W.-C. (2024). Development of chromium-impregnated sulfated silica as a mesoporous catalyst in the production of biogasoline from used cooking oil via a hydrocracking process. *Reaction Kinetics, Mechanisms and Catalysis*, 137, 971–989. DOI: 10.1007/s11144-024-02574-5.

[40] Hello, K.M., Hlial, E.K. (2019). Modification of silica with sulfuric acid and phosphoric acid for cellulose hydrolysis. *Journal of Physics: Conference Series*, 1294, 052013. DOI: 10.1088/1742-6596/1294/5/052013.

[41] Aneu, A., Wijaya, K., Syoufian, A. (2021). Silica-based solid acid catalyst with different concentrations of $H_2SO_4$ and calcination temperature: Preparation and characterization. *Silicon*, 13, 2265–2270. DOI: 10.1007/s12633-020-00741-6.

[42] Trisunaryanti, W., Larasati, S., Bahri, S., Ni'mah, Y.I., Efiyanti, L., Amri, K., Nuryanto, R., Sumbogo, S.D. (2020). Performance comparison of Ni–Fe loaded on $NH_2$-functionalized mesoporous silica and beach sand in the hydrotreatment of waste palm cooking oil. *Journal of Environmental Chemical Engineering*, 8, 104477. DOI: 10.1016/j.jece.2020.104477.

[43] Sie, S.T. (1992). Acid-catalyzed cracking of paraffinic hydrocarbons: Discussion of existing mechanisms and proposal of a new mechanism. *Industrial & Engineering Chemistry Research*, 31, 1881–1889. DOI: 10.1021/ie00008a008.

[44] Utami, M., Trisunaryanti, W., Shida, K., Tsushida, M., Kawakita, H., Ohto, K., Wijaya, K., Tominaga, M. (2019). Hydrothermal preparation of a platinum-loaded sulfated nanozirconia catalyst for the effective conversion of waste low-density polyethylene. *RSC Advances*, 9, 41392–41401. DOI: 10.1039/C9RA08834B.

[45] Saviola, A.J., Syoufian, A., Oh, W.-C., Wijaya, K. (2025). Atmospheric hydrotreatment of used palm cooking oil over nickel-dispersed phosphated zirconia as a highly stable nanocatalyst for bio-jet fuel production. *Inorganic Chemistry Communications*, 173, 113790. DOI: 10.1016/j.inoche.2024.113790.

[46] Cao, Z., Zhang, X., Mei, J., Guo, R., Wu, Z., Hou, S., Peng, S., Fan, S., Peng, C., Duan, A. (2022). Hydrocracking straight-run diesel into high-value chemical materials: The effect of acidity and kinetic study. *Industrial & Engineering Chemistry Research*, 61, 8685–8697. DOI: 10.1021/acs.iecr.2c00262.

[47] Singh, H.K.G., Yusup, S., Quitain, A.T., Abdullah, B., Ameen, M., Sasaki, M., Kida, T., Cheah, K.W. (2020). Biogasoline production from linoleic acid via catalytic cracking over nickel and copper-doped ZSM-5 catalysts. *Environmental Research*, 186, 109616. DOI: 10.1016/j.envres.2020.109616.

[48] Markowski, J., Imilkowski, P., Nowacki, M., Olejniczak, D., Madry, J., Netter, K., Jesionek, K., Wieczorkiewicz, G. (2020). The concept of measurement of calorific value of gaseous fuels. *E3S Web of Conferences*, 207, 01025. DOI: 10.1051/e3sconf/202020701025.

[49] Khaleel, O.J., Ismail, F.B., Ibrahim, T.K., Abu Hassan, S.H. (2022). Energy and exergy analysis of the steam power plants: A comprehensive review on the classification, development, improvements, and configurations. *Ain Shams Engineering Journal*, 13, 101640. DOI: 10.1016/j.asej.2021.11.009.

[50] Da Rocha Novaes, L., Secchi, A.R., Salim, V.M.M., De Resende, N.S. (2022). Enhancement of hydrotreating process evaluation: Correlation between feedstock properties, in-line monitoring and catalyst deactivation. *Catalysis Today*, 394, 390–402. DOI: 10.1016/j.cattod.2021.07.026.

[51] Zhou, J., Zhao, J., Zhang, J., Zhang, T., Ye, M., Liu, Z. (2020). Regeneration of catalysts deactivated by coke deposition: A review. *Chinese Journal of Catalysis*, 41, 1048–1061. DOI: 10.1016/S1872-2067(20)63552-5.

[52] Lahijani, P., Zainal, Z.A., Mohammadi, M., Mohamed, A.R. (2015). Conversion of the greenhouse gas $CO_2$ to the fuel gas CO via the Boudouard reaction: A review. *Renewable and Sustainable Energy Reviews*, 41, 615–632. DOI: 10.1016/j.rser.2014.08.034.

[53] Rambabu, K., Bharath, G., Sivarajasekar, N., Velu, S., Sudha, P.N., Wongsakulphasatch, S., Banat, F. (2023). Sustainable production of bio-jet fuel and green gasoline from date palm seed oil via hydroprocessing over tantalum phosphate. *Fuel*, 331, 125688. DOI: 10.1016/j.fuel.2022.125688.

[54] Ibrahim, M.A., El-Araby, R., Abdelkader, E., El Saied, M., Abdelsalam, A.M., Ismail, E.H. (2023). Waste cooking oil processing over cobalt aluminate nanoparticles for liquid biofuel hydrocarbons production. *Scientific Reports*, 13, 3876. DOI: 10.1038/s41598-023-30828-0.

[55] Hasanudin, H., Asri, W.R., Zulaikha, I.S., Ayu, C., Rachmat, A., Riyanti, F., Hadiah, F., Zainul, R., Maryana, R. (2022). Hydrocracking of crude palm oil to a biofuel using zirconium nitride and zirconium phosphide modified bentonite. *RSC Advances*, 12, 21916–21925. DOI: 10.1039/D2RA03941A.

[56] Widyastuti, Zulfa, L.L., Safrida, N., Ardhyananta, H., Triwicaksono, S., Kurniawansyah, F., Anintyasari, M., Ali, B.T.I., Raihan, J.N. (2024). Catalytic cracking of crude palm oil into biogasoline over HZSM-5 and USY-zeolite catalysts: A comparative study. *South African Journal of Chemical Engineering*, 50, 27–38. DOI: 10.1016/j.sajce.2024.07.009.

[57] Aulia, D., Maghfirah, A., Kadja, G.T.M. (2024). Green synthesis of hierarchical ZSM-5 using cellulose nanocrystal-mesoporogen at low temperature for catalytic cracking of palm oil into aromatic-rich gasoline. *Results in Engineering*, 24, 102954. DOI: 10.1016/j.rineng.2024.102954.